The Astrophysical Journal, 672:1209–1220, 2008 January 10

MODELING NONPOTENTIAL MAGNETIC FIELDS IN SOLAR ACTIVE REGIONS

M. G. Bobra, A. A. van Ballegooijen, and E. E. DeLuca
Harvard-Smithsonian Center for Astrophysics, Cambridge, MA 02138
Received 2007 March 9; accepted 2007 September 25

ABSTRACT

Electric currents are present in the coronae above solar active regions, producing nonpotential magnetic fields that can be approximated as nonlinear force-free fields (NLFFFs). In this paper NLFFF models for two active regions observed in 2002 June are presented. The models are based on magnetograms from *SOHO* MDI and are constrained by nonpotential structures seen in BBSO Hα images and *TRACE* EUV images. The models are constructed using the flux rope insertion method. We find that the axial fluxes of the flux ropes are well constrained by the observations. The flux ropes are only weakly twisted, and electric currents flow mainly at the interface between the flux rope and its surroundings. In one case, the flux rope is anchored with both ends in the active region; in the other case, the flux rope extends to the neighboring quiet Sun. We find that the magnetic fields in these active regions are close to an eruptive state: the axial flux in the flux ropes is close to the upper limit for eruption. We also derive estimates for magnetic free energy and helicity in these regions.

Subject headings: Sun: corona — Sun: magnetic fields

1. INTRODUCTION

It is generally agreed that solar flares represent the release of magnetic free energy stored in the corona prior to the flare (Priest & Forbes 2002). Photospheric vector fields in active regions can deviate significantly from a potential field (e.g., Gary et al. 1987; Pevtsov et al. 1995, 1997), and sheared magnetic fields are often observed in the corona prior to flares (Acton et al. 1992; Rust & Kumar 1996; Canfield et al. 1999; Sterling et al. 2000). The study of solar flares and other eruptive phenomena requires that we understand how magnetic energy is stored in the preflare corona. Some of the key questions are as follows: (1) What is the three-dimensional (3D) structure of magnetic fields and electric currents in the preflare corona, and how much free energy is stored in the field? (2) What are the evolutionary processes by which the magnetic free energy is built up? (3) How is the energy released during a flare? In this paper we focus on the first question, namely, the structure of nonpotential fields in active regions.

Schrijver et al. (2005) studied the nonpotentiality of active regions using magnetograms from the Michelson Doppler Imager (MDI) on the *Solar and Heliospheric Observatory* (*SOHO*; Scherrer et al. 1995) and extreme-ultraviolet (EUV) images from the *Transition Region and Coronal Explorer* (*TRACE*; Handy et al. 1999). They found that significant nonpotentiality occurs when new magnetic flux has recently emerged into the corona, or when rapidly evolving, opposite polarity flux concentrations are in close contact. Flares are found to occur more frequently in active regions with nonpotential coronae than in potential regions. Schrijver (2007) analyzed observations of X- and M-class flares and found that, without exception, large flares are associated with regions where there is a strong gradient of the photospheric magnetic field across the polarity inversion line (PIL). He proposed that the emergence of current-carrying magnetic field causes most, if not all, major flares.

The magnetic pressure in the active corona is generally much larger than the gas pressure. Therefore, except during a flare or eruption, the corona is nearly force-free, $\boldsymbol{j} \times \boldsymbol{B} \approx 0$, where $\boldsymbol{B}(\boldsymbol{r})$ is the magnetic field and $\boldsymbol{j}(\boldsymbol{r})$ is the electric current density. This implies $\nabla \times \boldsymbol{B} \approx \alpha \boldsymbol{B}$, where $\alpha(\boldsymbol{r})$ varies among different field lines yet is constant for any particular field line. A magnetic field with this property is called a nonlinear force-free field (NLFFF). Several authors have developed numerical methods for reconstructing NLFFFs by extrapolating photospheric vector fields into the corona, including the "evolutionary" method (Mikic & McClymont 1994), the current field iteration method (Bleybel et al. 2002; Régnier et al. 2002; Wheatland 2006), the magnetofrictional method (Valori et al. 2005), and various optimization methods (Wheatland et al. 2000; Wiegelmann 2004; Wiegelmann et al. 2006). Measurements of photospheric vector fields and their use in extrapolation are subject to a number of uncertainties (see McClymont et al. 1997). Recently, Schrijver et al. (2006) and Metcalf et al. (2007) performed various tests of such extrapolation methods.

In the present paper we construct NLFFF models for two active regions, using a method that does not require observed vector fields. Instead, we use the flux rope insertion method (van Ballegooijen 2004; van Ballegooijen et al. 2007), which only requires line-of-sight magnetograms. The models are constrained by *TRACE* observations of nonpotential structures in coronal loops and by the observed Hα filaments. The purpose of this modeling is to understand the 3D structure of magnetic fields and electric currents in these active regions. The models only give the coronal structure at one instant of time, so we cannot address the question of how the nonpotential structures are formed. Nevertheless, such modeling can provide important insights regarding the distribution of electric currents within the flux rope and the overall stability of the coronal field.

The paper is organized as follows. Section 2 describes how the observational data are selected, and § 3 describes how the NLFFF models are constructed (for details see Appendix A). The modeling results are described in §§ 4 and 5. The conclusions are presented in § 6.

2. OBSERVATIONS

Three sets of observational data were used in this study: line-of-sight magnetograms from *SOHO* MDI, full-disk Hα images from Big Bear Solar Observatory (BBSO), and Fe IX/X 171 Å images from *TRACE*. The full-disk MDI magnetograms have a spatial resolution of about 4″, and the high-resolution magnetograms

TABLE 1
Observed Active Regions

Parameter	Data Set 1	Data Set 2
Date	2002 Jun 18	2002 Jun 23
Time (UT)	15:47	16:00
Magnetograms[a]	5 HR	1 FD + 5 HR
NOAA active regions	9997, 10000	10005
AR latitude (deg)	+13	+13
Positive magnetic flux (10^{22} Mx)	+2.5	+2.4
Negative magnetic flux (10^{22} Mx)	−1.7	−2.4
Filament chirality	Dextral	Dextral
Filament length (Mm)	260	>280

[a] Number of MDI magnetograms used (FD = full disk, HR = high resolution).

have a spatial resolution of about 1.25″ with a field of view (FOV) of 11′ × 11′ centered approximately 160″ north of the equator (Scherrer et al. 1995). The BBSO Hα images have a spatial resolution of about 2″. The *TRACE* images have a 512″ × 512″ FOV with a spatial resolution of about 1″ (Handy et al. 1999). These data represent the solar magnetic field configuration at the photosphere, chromosphere, and corona, respectively.

Observational data were selected based on the following criteria. First, the target active region must be located near disk center, must contain one or more Hα filaments, and must be in a nonflaring state. Second, nearly simultaneous image data from *TRACE*, BBSO, and *SOHO* MDI must be available. Third, the *TRACE* images must show nonpotential coronal loop structures. In nonflaring active regions, the most prominent features seen in *TRACE* images are bright rays emanating from the sunspots or other magnetic elements in the active region. These structures usually do not show much evidence for nonpotentiality. The areas near the PIL are usually devoid of bright EUV loops crossing the PIL. However, on closer inspection one often sees thin, faint loops that run parallel to the PIL and appear to be associated with the observed filament. The emission and mass flow along these highly sheared loops are transient, but the underlying magnetic field appears to be stable. We used movie sequences to identify such features in a few active regions. We suspect that faint, highly sheared loops are present in many active regions that contain Hα filaments.

The above criterion for nonpotentiality is different from the one used by Schrijver et al. (2005), who compare the *TRACE* images with potential field models. Those authors give more weight to the correspondence of direction patterns of field lines with long loops in the outer perimeter of the active region corona, and loops emanating from sunspots. Here we focus attention on low-lying, sheared magnetic fields associated with filaments.

Two data sets were selected for detailed analysis and modeling. Data set 1 was taken on 2002 June 18 and contains a younger active region (NOAA 10000) that has emerged into an older, more dispersed region (NOAA 9997). Data set 2 is for NOAA 10005 observed 5 days later. Some parameters of the active regions and filaments are listed in Table 1. In both cases the active regions are close to the central meridian. The magnetic fluxes listed in Table 1 are the photospheric fluxes of each polarity; for data set 1 these fluxes are the combined values for NOAA 9997 and NOAA 10000 (note that there is a significant flux imbalance).

In both cases the active regions show evidence of nonpotentiality due to the presence of sheared loops observed in the *TRACE* data. However, according to the definition by Schrijver et al. (2005), data set 1 would likely be defined as potential, as the peripheral active region loops align closely with a potential field model, whereas data set 2 would likely be defined as nonpotential, as the peripheral active region loops do not align closely with a potential field model. The observations and analyses are discussed in more detail in §§ 4 and 5.

3. FLUX ROPE INSERTION METHOD

In previous work we developed a method for constructing NLFFF models of solar active regions and filaments (van Ballegooijen 2004; van Ballegooijen et al. 2007). The method involves inserting a magnetic *flux rope* into a potential field model of an active region. The potential field represents the coronal arcade that overlies the flux rope and prevents it from erupting into the heliosphere. The computation involves magnetofrictional relaxation (Yang et al. 1986; van Ballegooijen et al. 2000) to drive the magnetic field toward a force-free state, while preserving the topology of the magnetic field lines. In the present paper we use an improved version of the flux rope insertion method. The new method is described in Appendix A; a brief summary is given below.

The computational domain is a wedge-shaped volume in the corona surrounding an observed active region and filament. The domain extends from the photosphere to a "source surface" at a radial distance of about 2 $R_\odot$ from Sun center. The magnetic field $\boldsymbol{B}(\boldsymbol{r})$ in this volume is described using vector potentials in spherical geometry. First a modified potential field is computed, based on observations of the photospheric magnetic field. Then a flux rope is inserted into the field at the location of an observed Hα filament. The field is then evolved in time according to the magnetic induction equation, while keeping the radial field in the photosphere fixed. In the corona, the plasma velocity is assumed to be proportional to the Lorentz force (magnetofriction), so that the field evolves toward a nonlinear force-free state, if one exists. In the photosphere, an additional upward force is added to simulate the effects of magnetic buoyancy on photospheric flux tubes (see Metcalf et al. 2007).

A new feature of the code used here is that the induction equation includes hyperdiffusion, a type of magnetic diffusion that preserves magnetic helicity (see Boozer 1986; Bhattacharjee & Hameiri 1986). The purpose of this diffusion is to suppress the buildup of numerical artifacts in the coronal electric current distribution, thus improving the accuracy of the Lorentz force calculation. The rate of hyperdiffusion is small, so that the topology of the coronal field is more or less preserved during the relaxation process.

The end result of the relaxation is a 3D NLFFF model of the magnetic field $\boldsymbol{B}(\boldsymbol{r})$ with a magnetic flux rope located at the location of the observed Hα filament. The magnetic energy and helicity are also computed as described in Appendix B. We then repeat the above process for different values of the axial flux $\Phi_{\rm axi}$ and the poloidal flux $F_{\rm pol}$ of the flux rope (these parameters are varied manually, not using an automated procedure). The purpose is to find the solution that best fits the observed coronal structure as revealed by *TRACE* and BBSO images.

4. RESULTS FOR NOAA 9997/10000

Data set 1 shows a younger active region (NOAA 10000) that has emerged into an older, more dispersed region (NOAA 9997). On 2002 June 18 both regions are close to the central meridian. Figure 1 shows BBSO and *TRACE* images taken at 15:47 UT, together with a *SOHO* MDI magnetogram. NOAA 10000 is the smaller bipole in the upper left quadrant of each frame. The Hα image (Fig. 1*a*) shows a dark filament along the PIL that runs through both active regions. The filament can also be seen in the *TRACE* image (Fig. 1*c*), especially near the bend in the filament

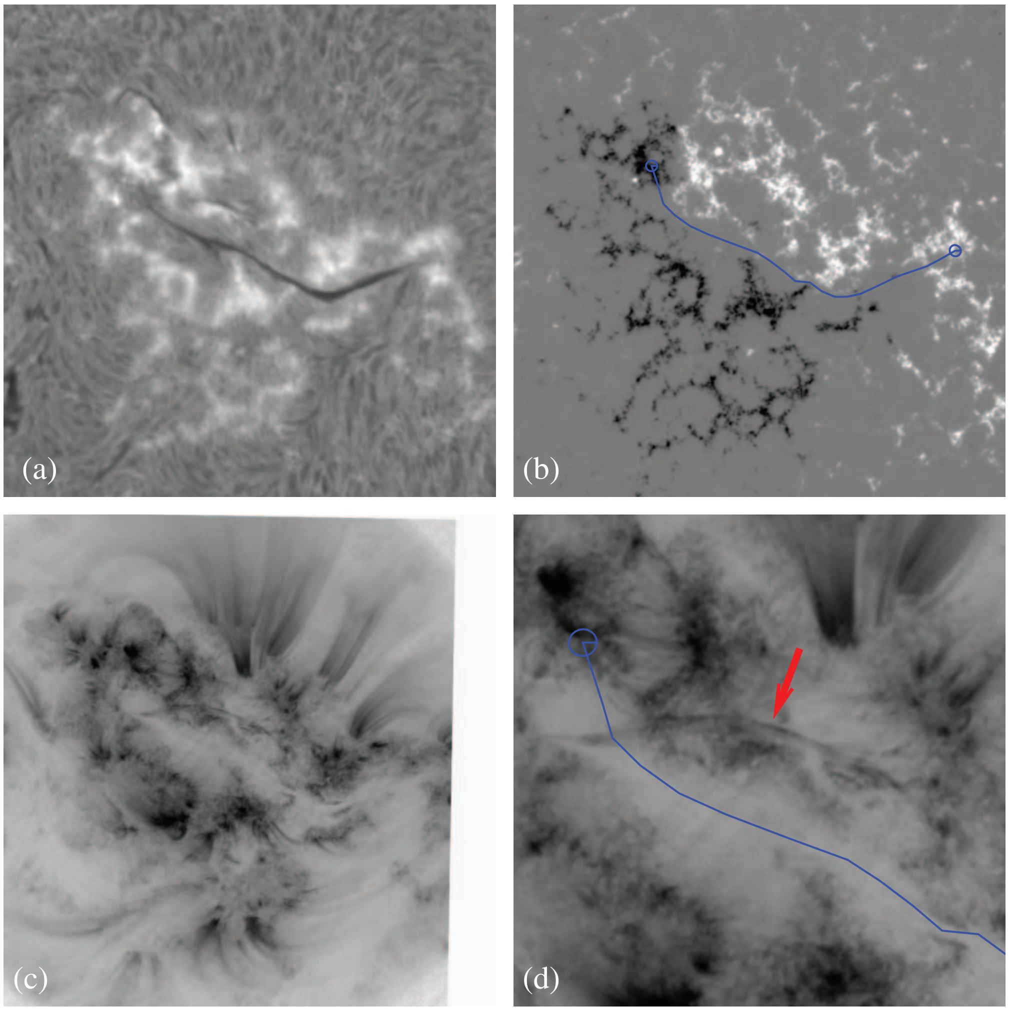

Fig. 1.—Active regions NOAA 9997 and NOAA 10000 on 2002 June 18 at 15:47 UT: (*a*) Hα image from BBSO; (*b*) MDI magnetogram with selected path of the flux rope (*blue line*); (*c*) *TRACE* 171 Å image. The FOV in panels (*a*)–(*c*) is 0.5 $R_\odot$; north is up, and west is to the right. (*d*) Close-up of sheared coronal loop that crosses the inversion line.

(note that the *TRACE* image is shown as a negative, so bright features are black in this image). Figure 1*b* shows that the filament originates in positive polarity flux on the western side of NOAA 9997 and ends in the negative flux of NOAA 10000. Therefore, the axial field of the filament is directed to the east and has *dextral* orientation with respect to the neighboring positive polarity flux (see Martin et al. 1994).

The *TRACE* image shows many bright rays emanating from magnetic elements on either side of the PIL, which are consistent with a potential field model. Thus, this active region would likely be defined as potential by Schrijver et al. (2005). However, one loop crosses the PIL. The loop is a transient feature; it is formed by injection of material from a small flare that occurred to the north of the PIL starting at about 15:28 UT. The small flare does not appear to disturb the flux rope. Figure 1*d* shows a close-up of this loop. The western part of the loop runs parallel to the PIL, and the eastern part crosses the PIL at about 45°, suggesting that it is part of the sheared magnetic field overlying the filament. Indeed, the direction of magnetic shear as indicated by this loop is consistent with the eastward direction of the magnetic field in the filament.

We constructed a series of models with different values of the axial and poloidal fluxes of the flux rope. The model parameters are listed in Table 2. All models use variable grid spacing with 400×384 cells on the photosphere and a cell size $\Delta\phi = 1.5 \times 10^{-3}$ $R_\odot$ (see Appendix A). Model 0 is a reference model in which electric currents are present only in the photosphere (see Appendix A), i.e., it is a potential field in the corona. Some of the models converge toward an NLFFF equilibrium state, while others do not converge and the flux rope slowly lifts off. The degree of convergence is shown in the fourth column of Table 2: "Y" indicates that the model is well converged to an NLFFF, "N"

TABLE 2
Model Parameters for NOAA 9997/10000

Model	$\Phi_{\rm axi}$ (10^{20} Mx)	$F_{\rm pol}$ (10^{10} Mx cm^{-1})	NLFFF	E_c (10^{32} ergs)	H_R (10^{43} Mx^2)
0.............	...	...	Y	5.17	0.0
1.............	4	−1	Y	5.67	−1.03
2.............	7	−1	Y	6.15	−1.82
3.............	10	−1	Y	6.59	−2.60
4.............	15	−1	?	7.34	−3.92
5.............	20	−1	N	...	...
6.............	30	−1	N	...	...
7.............	10	−10	Y	8.45	−3.16
8.............	(4, 10)	(−1, −1)	Y	6.70	−2.72
9.............	(4, 12)	(−1 ,−1)	N	...	...

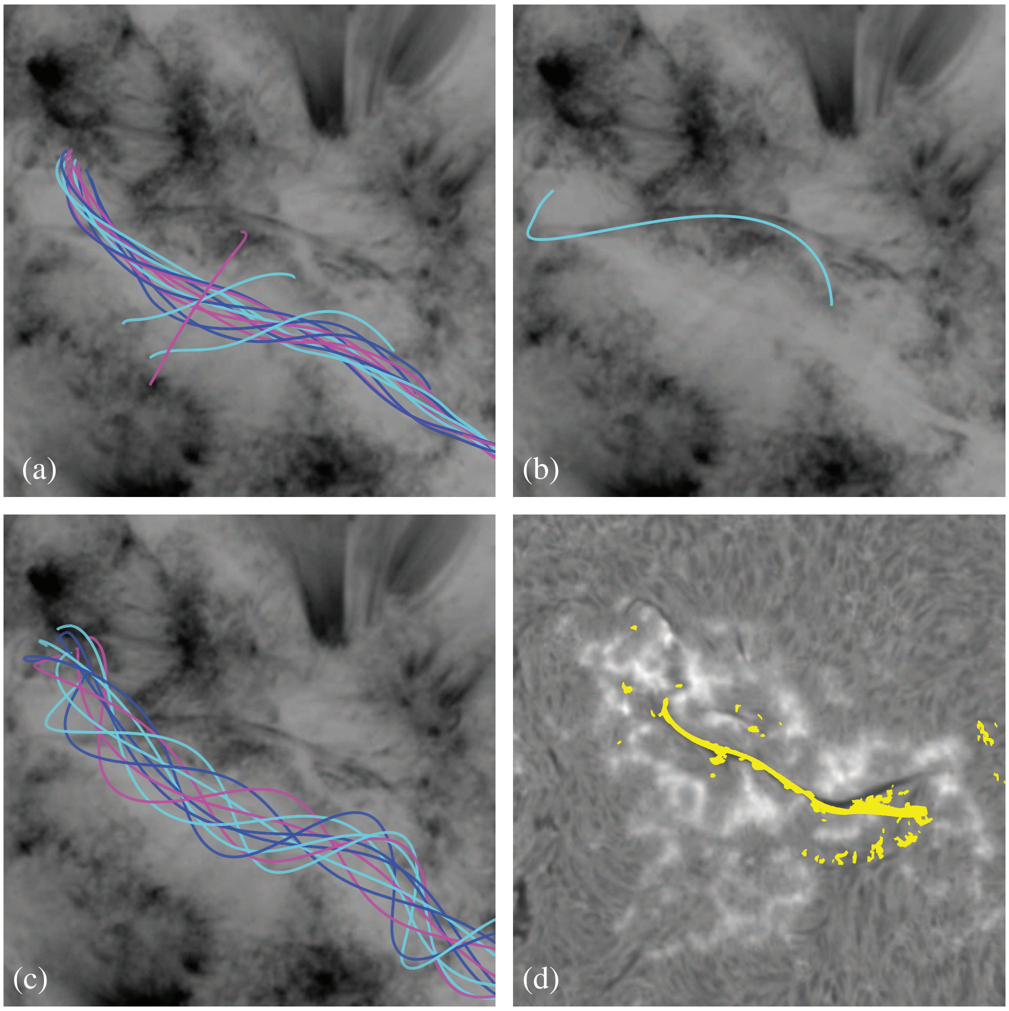

Fig. 2.—Models of NOAA 9997/10000 in which the axial flux of the flux rope is constant along the filament. (*a*) Field lines from model 1 overlaid on the *TRACE* 171 Å image. Note that the flux rope is too narrow to reproduce the observed loop. (*b*) Model 4 reproduces the observed loop quite well, but this model is near the threshold of instability. (*c*) In model 7 the field lines are highly twisted and do not match the observed loop. The FOV in panels (*a*)–(*c*) is 0.2 $R_\odot$; north is up, and west is to the right. (*d*) Hα image with overlay of field line dips (*yellow*) for model 7 (FOV: 0.5 $R_\odot$).

indicates liftoff, and a question mark indicates that even after 20,000 iterations it is unclear whether the model is stable or unstable.

We first consider models with a single flux rope (models 1–7). In this case the axial magnetic flux $\Phi_{\rm axi}$ is constant along the flux rope. The assumed path of the flux rope is shown in Figures 1*b* and 1*d* and coincides with the observed filament. Models 1–6 use a low value for the poloidal flux, $F_{\rm pol} = -10^{10}$ Mx cm^{-1}, which produces a weakly twisted, left-helical flux rope. We find that for small values of axial flux the flux rope is too slender to reproduce the observed *TRACE* loop. This is illustrated in Figure 2*a*, which shows the field configuration for model 1 with $\Phi_{\rm axi} = 4 \times 10^{20}$ Mx. In this model, the sheared field is located close to the PIL, and field lines somewhat farther away from the PIL do not have enough magnetic shear to reproduce the observed loop. As the axial flux is increased, the width of the flux rope increases. In model 4, the width of the flux rope approaches the value needed to reproduce the observed loop (see Fig. 2*b*). However, this model is only marginally stable. If the axial flux is further increased (models 5 and 6), the magnetofrictional code no longer reaches an equilibrium state: the flux rope keeps expanding and moving radially outward, especially in the western part of the flux rope where the photospheric field is very weak on the southern side of the filament. Therefore, the models with a single flux rope and $F_{\rm pol} = -10^{10}$ Mx cm^{-1} do not produce a good NLFFF that fits the *TRACE* data.

We also tried models with larger poloidal flux. Figure 2*c* shows the magnetic configuration for model 7, which has $F_{\rm pol} = -10^{11}$ Mx cm^{-1} and $\Phi_{\rm axi} \approx 10 \times 10^{20}$ Mx. In this case the flux rope is more strongly twisted, but the rope is again not wide enough to reproduce the observed *TRACE* loop. Figure 2*d* shows the locations of dips in the field lines, i.e., sites where the field lines are horizontal and curved upward. It has long been suggested that filament plasma is located at such dips in the field lines (e.g., Aulanier & Démoulin 1998). However, others have argued that dips are not necessary for a filament to form (e.g., Antiochos et al. 2000; Karpen et al. 2001, 2005). Due to the strong twist, there are dips along the entire length of the modeled flux rope, but in the western part of the active region the flux rope is significantly displaced from the observed filament (see Fig. 2*d*). This displacement is due to the fact that the photospheric fields on the northern side of the filament are stronger than those on the southern side, therefore the flux rope is pushed to the south. The field is only marginally stable; for larger axial fluxes the flux rope is no longer in equilibrium. Therefore, models with large poloidal flux do not reproduce the observed filament, nor the *TRACE* loop.

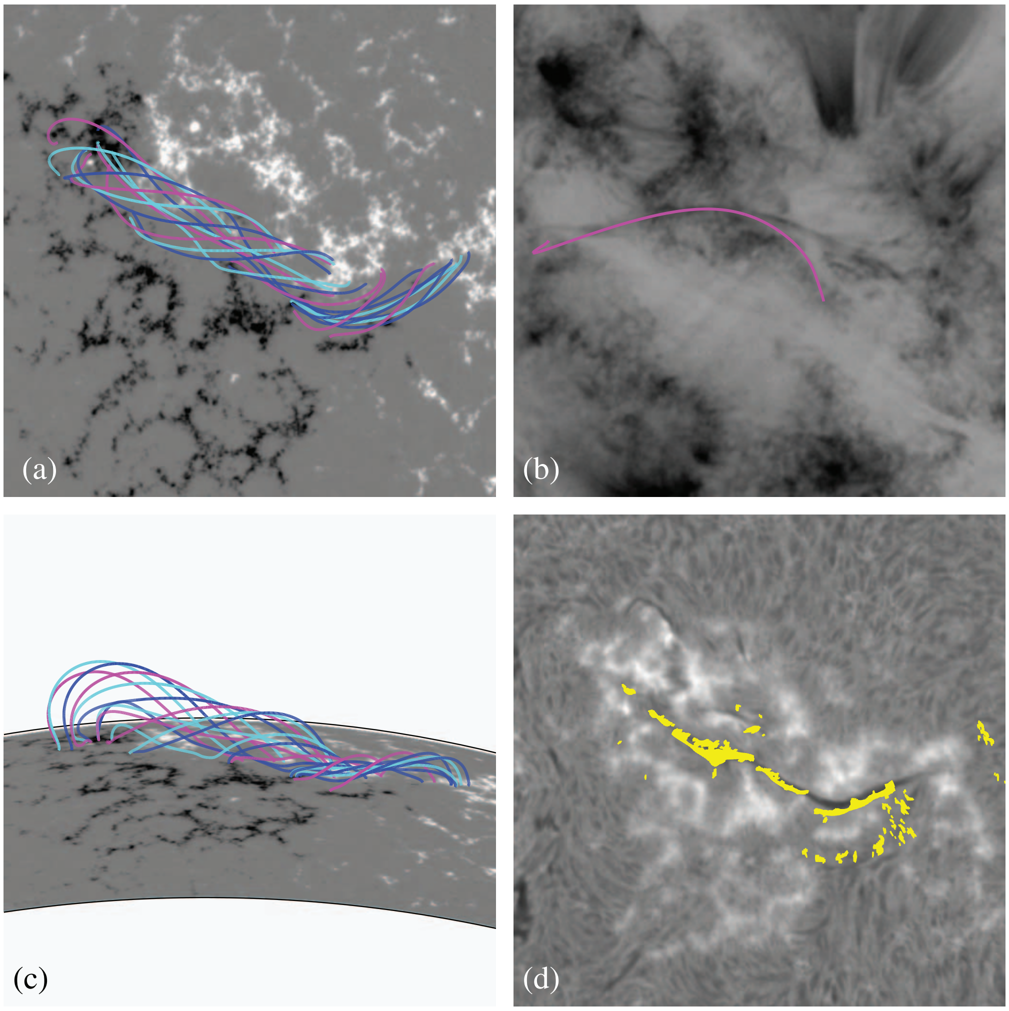

FIG. 3.—Results for a model in which the axial flux varies along the flux rope (model 8). (*a*) Photospheric magnetic field and selected field lines near the edge of the flux rope (FOV: 0.5 $R_\odot$). (*b*) *TRACE* 171 Å image (FOV: 0.5 $R_\odot$) with field line that most closely matches the sheared coronal loop. (*c*) Magnetic configuration as seen from latitude $-62°$. (*d*) Hα image with overlay of field line dips (*yellow*). North is up, west is to the right.

The basic problem with the above models is that the axial flux is constant along the filament. The axial flux necessary to reproduce the observed *TRACE* loop (about 15×10^{20} Mx) is too large to produce equilibrium in the western part of the flux rope. Therefore, we also consider two cases in which the axial flux varies along the length of the filament (models 8 and 9). These models are constructed by inserting two flux ropes into the magnetic structure, one that starts at the western end of the observed filament, and another that starts farther to the east, in the positive polarity flux just north of the bend in the filament. In the eastern part of the active region the two flux ropes follow more or less the same path, so their axial fluxes combine into a single flux rope (for model 8, $\Phi_{\rm axi} = 14 \times 10^{20}$ Mx). In the western part only the first flux rope contributes ($\Phi_{\rm axi} = 4 \times 10^{20}$ Mx), so the flux rope is much less susceptible to liftoff than in model 4. The parameters of the flux ropes are listed in Table 2.

Results for model 8 are shown in Figures 3, 4, and 5. In Figures 3*a* and 3*c* we show selected field lines located near the edge of the flux rope. Figure 3*b* shows a close-up of the *TRACE* loop and the model field line that best fits the observed loop. Figure 3*d* shows the locations of dips in the field lines. Note that, unlike in model 7 (Fig. 2*d*), the dips follow the observed filament in the western part of the active region. Therefore, model 8 provides the best fit to both the *TRACE* and BBSO data. Figures 4*a* and 4*b* show the distributions of radial magnetic field and electric current at grid level $z = 4$, which corresponds to a height of 4.2 Mm above the photosphere. We chose this height because it cuts through the lower part of the flux rope. Figure 4*a* shows that B_r at this height is more smoothly distributed than B_r in the photosphere (compare with Fig. 3*a*) but still has significant fine-scale structure. Figure 4*b* shows the distribution of the radial electric currents, j_r; the currents flow upward on the southern side of the flux rope ($j_r > 0$) and downward on the northern side ($j_r < 0$). Note that the currents are concentrated at the edge of the flux rope.

Active regions generally have a complex magnetic structure consisting of multiple magnetic flux systems separated by quasi-separatrix layers (QSLs; see Démoulin et al. 1996). These QSLs may be important for understanding how the solar corona is heated. Figures 4*c* and 4*d* show the QSL structure for NOAA 9997/10000 as predicted by our models. These figures show the intersection of the QSLs with a horizontal surface $z = 4$. Plotting the QSLs at some height makes the results less sensitive to conditions at a lower boundary, where the electric currents are not well resolved. Figure 4*c* shows the QSLs for model 8, and Figure 4*d* shows the corresponding diagram for the potential field (model 0). In these panels the horizontal surface is divided into three areas: blue for closed magnetic fields, green for open fields, and orange for fields that intersect the side boundaries. Following Démoulin

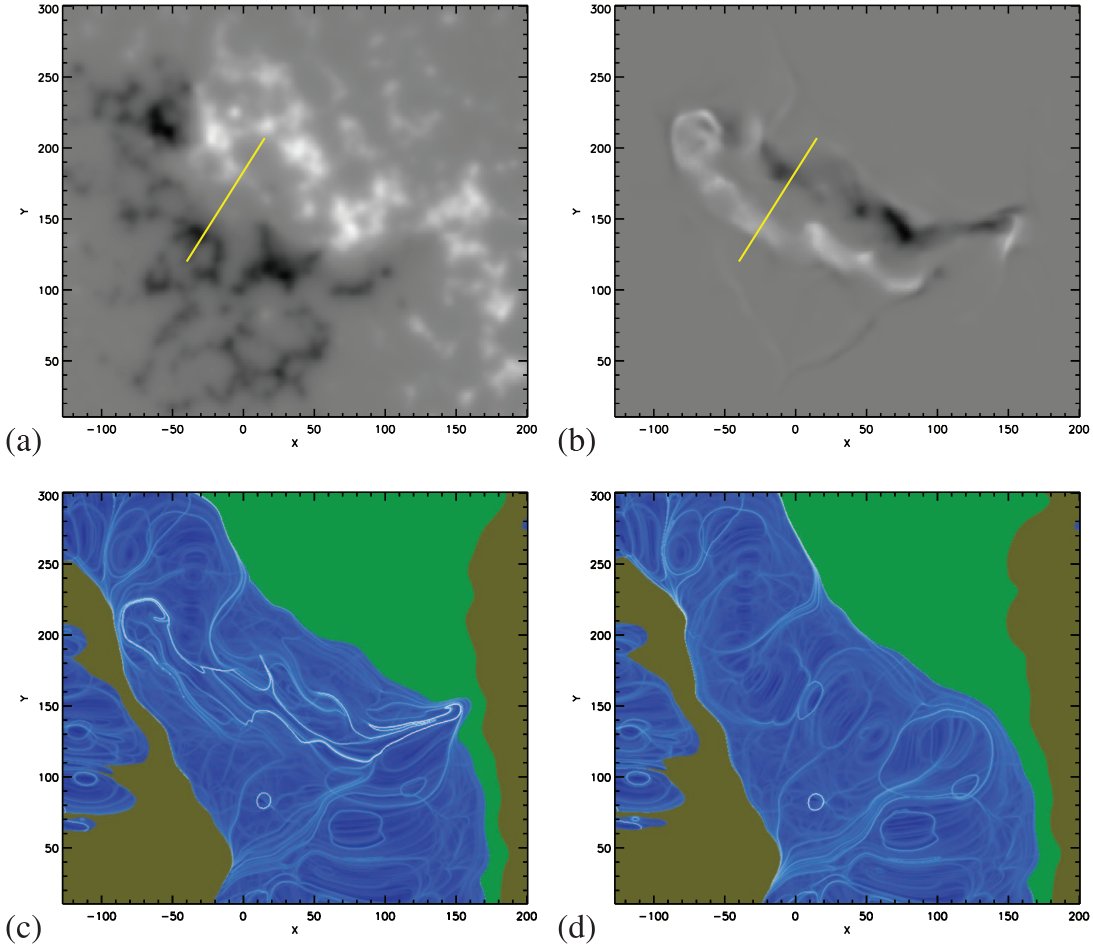

FIG. 4.—Magnetic field, electric currents, and QSLs at a height of 4.2 Mm ($z = 4$) in model 8. (*a*) Radial component of magnetic field, $B_r(x, y, 4)$. (*b*) Radial component of current density, $j_r(x, y, 4)$. (*c*) Quantity $N(x, y, 4)$ showing the location of QSLs (see text). (*d*) Same quantity for the potential field (model 0).

et al. (1996), the brightness in the blue area is proportional to the quantity

$$N(x, y) \equiv \sqrt{\left(\frac{\partial X}{\partial x}\right)^2 + \left(\frac{\partial X}{\partial y}\right)^2 + \left(\frac{\partial Y}{\partial x}\right)^2 + \left(\frac{\partial Y}{\partial y}\right)^2}, \quad (1)$$

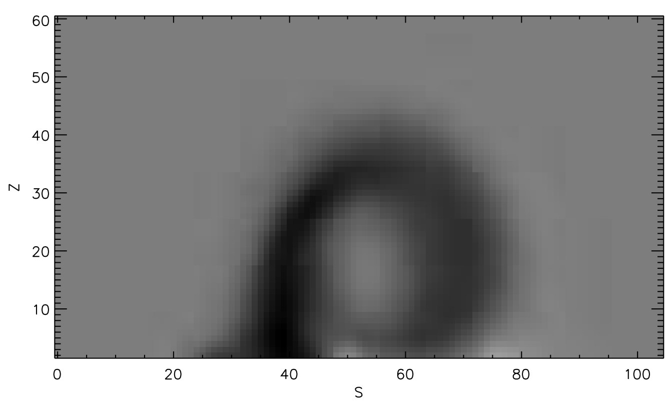

FIG. 5.—Hollow core distribution of electric currents in a vertical cross section of the flux rope (model 8). The location of the vertical plane is shown by the yellow line in Figs. 4*a* and 4*b*. The coordinates are in units of the cell size, which is about 1 Mm on the Sun.

where $(x, y, 4)$ are the coordinates of a point at level $z = 4$, $(x', y', 0)$ and $(x'', y'', 0)$ are the two footpoints of the closed field line that passes through $(x, y, 4)$, and $X \equiv x'' - x'$ and $Y \equiv y'' - y'$ measure the relative position of the footpoints.

Figure 4 shows that QSLs are present in both the potential and NLFFF models, but the structure of the QSLs is different in the two models. The structure of the QSLs for the potential field and that for the NLFFF are very similar away from the flux rope. The potential field determines the large-scale connectivity of the region, where the fields are open and where long loops leave the computational domain. The QSLs in the NLFFF calculation show the location of the edge of the flux rope. This region, where field lines change from being aligned with the flux rope to overlying the flux rope, is important for studying the heating and stability of the filament. We note that the QSL shape is very similar to the shape of the vertical current (although substantially thinner). This relationship is expected and consistent. Specialized time-dependent codes will be needed to evaluate the relationship of the QSLs to flux rope heating and the observational signatures in a particular instrument. At this time, we cannot directly compare the influence of the model currents on EUV or X-ray coronal emission, or test QSL heating models by comparing them with observations. Our models provide needed input to that type of calculation, but the calculations themselves are beyond the scope of this work.

The distribution of electric currents within the flux rope is likely to be important for understanding how the field becomes unstable

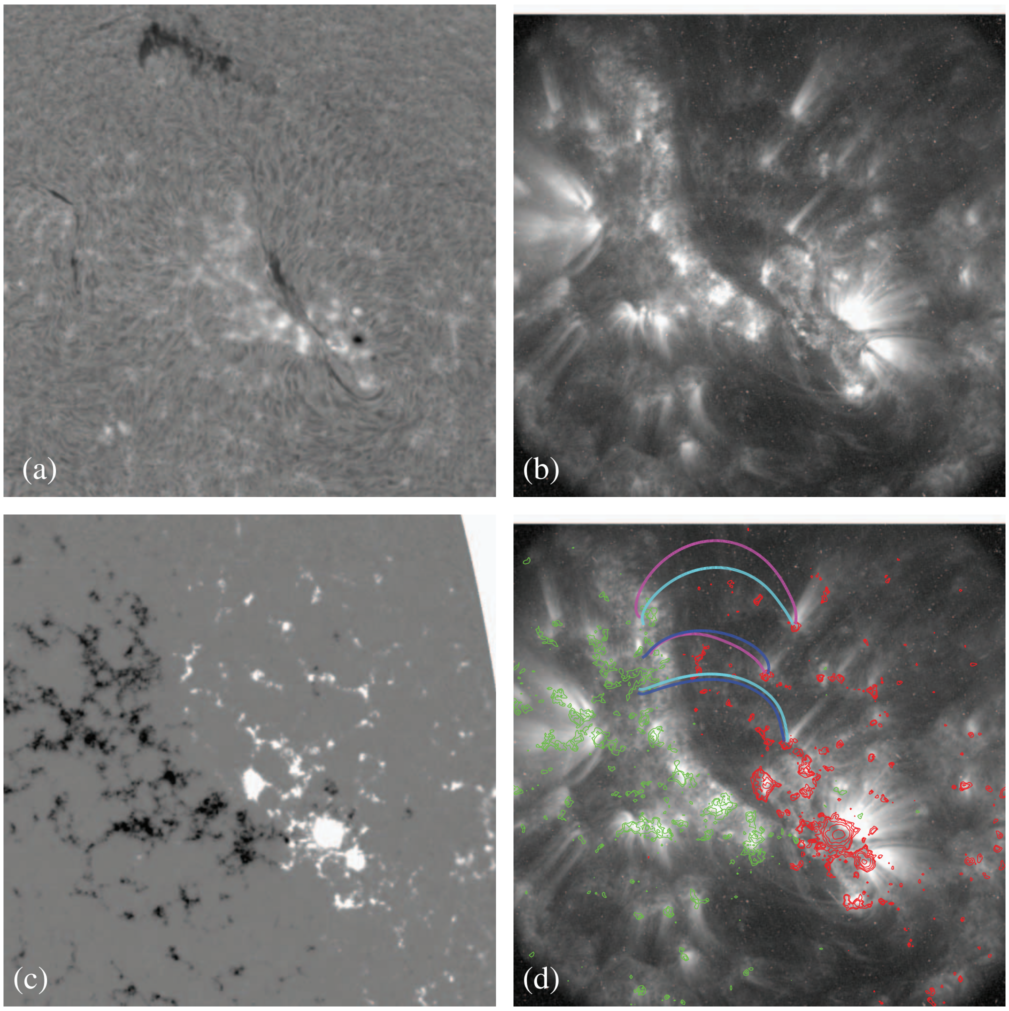

FIG. 6.—Active region NOAA 10005 on 2002 June 23 at 16:00 UT: (*a*) Hα image with FOV of 0.8 $R_{\odot}$ extracted from full-disk BBSO image; (*b*) *TRACE* 171 Å image with FOV of 0.5 $R_{\odot}$; (*c*) co-aligned MDI magnetogram; (*d*) *TRACE* image with contours from MDI magnetogram and field lines from potential field model. North is up, and west is to the right.

in a flare or CME. Figure 5 shows the current distribution in a vertical cross section of the flux rope for model 8 (the location of this vertical plane is indicated by yellow lines in Figs. 4*a* and 4*b*). The quantity plotted in Figure 5 is the component of $\boldsymbol{j}$ perpendicular to this vertical plane, i.e., parallel to the flux rope axis, which intersects the plane at $s \approx 55$, $z \approx 17$ in this figure. Note that the largest currents occur at the interface between the flux rope and its local surroundings (dark ring in Fig. 5). The current density on the axis is much lower than that at the edge; i.e., the currents have a *hollow core* distribution. This is a consequence of the fact that in model 8 the flux rope is only weakly twisted. In contrast, in model 7 the current density peaks on the axis. Since model 8 is a better fit to the BBSO and *TRACE* observations, we conclude that hollow core distributions of current indeed exist on the Sun. Figure 5 also shows that the regions farther away from the flux rope are again nearly current-free ($\boldsymbol{j} \approx 0$). In reality, the current density may drop off more gradually with height above the flux rope.

Finally, we construct model 9 with a slightly larger value for the axial magnetic flux in the flux rope compared to model 8 (see Table 2). After 20,000 iterations it is clear that the field expands and does not reach an equilibrium state. Therefore, the upper limit on the axial flux that can be confined within this active region is about 15×10^{20} Mx, and model 8 is close to this upper limit. Since model 8 gives the best fit to the *TRACE* and BBSO data, we conclude that the flux rope in NOAA 9997/10000 is close to an eruptive state. A slight increase in the axial flux (e.g., by flux cancellation at the PIL) will produce an eruption. The GOES X-ray data indicate that no large flares occurred in these active regions within several days of the time of the present model (an M-class flare occurred on June 23 as the region approached the west limb). Therefore, the flux rope appears to have been stable for several days.

5. RESULTS FOR NOAA 10005

In this section we present models for active region NOAA 10005 observed on 2002 June 23 and 24. Figure 6 shows various images of the active region. The Hα image (Fig. 6*a*) shows two active region filaments, a curved filament to the south of the leader spot, and a longer one located along the main PIL of the active region. The second filament is located in a filament channel that starts near the leader spot and extends into the quiet Sun to the north of the active region. The large quiescent filament seen near the top of Figure 6*a* may also be located in this channel. Note that there is a large-scale pattern in the alignment of the chromospheric fibrils in and around the active region. In the northwestern part of the region the fibrils are pointed in a northwesterly direction.

Figure 6*b* shows the *TRACE* 171 Å image from 16:05 UT (note the difference in scale from Fig. 6*a*). There are bright rays emanating from the sunspots and other magnetic elements in the

TABLE 3
Model Parameters for NOAA 10005

Model	$\Phi_{\rm axi}$ (10^{20} Mx)	$F_{\rm pol}$ (10^{10} Mx cm^{-1})	NLFFF	E_c (10^{32} ergs)	H_R (10^{43} Mx^2)
10	...	...	Y	8.41	0.0
11	(2.3, 13.7)	(−1, −2)	Y	10.35	−2.61
12	(2.3, 22.0)	(−1, −3)	N	...	...

active region. These rays are thought to be the ends of coronal loops that are much longer than the observed rays; only the ends of these loops are visible because the Fe IX/X emission drops off rapidly with height. In the northwestern part of the active region, the rays have the same northwesterly direction as the chromospheric fibrils. Figure 6*c* shows the MDI magnetogram that was used to construct 3D magnetic models. An overlay of the magnetogram onto the *TRACE* image is shown in Figure 6*d*, together with selected field lines from a potential field model (model 10). Note that in the northwestern part of the active region the projected field lines do not follow the observed EUV rays and chromospheric fibrils. Therefore, the magnetic configuration is not accurately modeled by a potential field. Thus, the active region appears to be an example of a "nonpotential" region as defined by Schrijver et al. (2005).

We constructed various models of NOAA 10005; the model parameters are listed in Table 3. The models use variable grid spacing with 400×480 cells on the photosphere and a cell size $\Delta\phi = 2 \times 10^{-3}\ R_\odot$ (see Appendix A). Model 10 is again a reference model in which electric currents are present only in the photosphere; i.e., it is a potential field in the corona. Models 11 and 12 were obtained by inserting flux ropes along the paths of the two observed filaments. The model that best reproduces the observations is model 11.

Results for model 11 are shown in Figure 7. The computational domain is larger than the area shown in the figure and extends to a latitude of +48°. Figure 7*a* shows selected field lines traced in the 3D model. The model reproduces the *TRACE* loop that overlies the curved filament to the south of the sunspot. Other field lines follow the main flux rope that starts in the spot and extends all the way to the north of the active region. At higher latitude (not shown), some of these field lines are open, while others exit the computational domain through its western boundary. The modeled field at high latitude is still slowly evolving even after 30,000 iterations

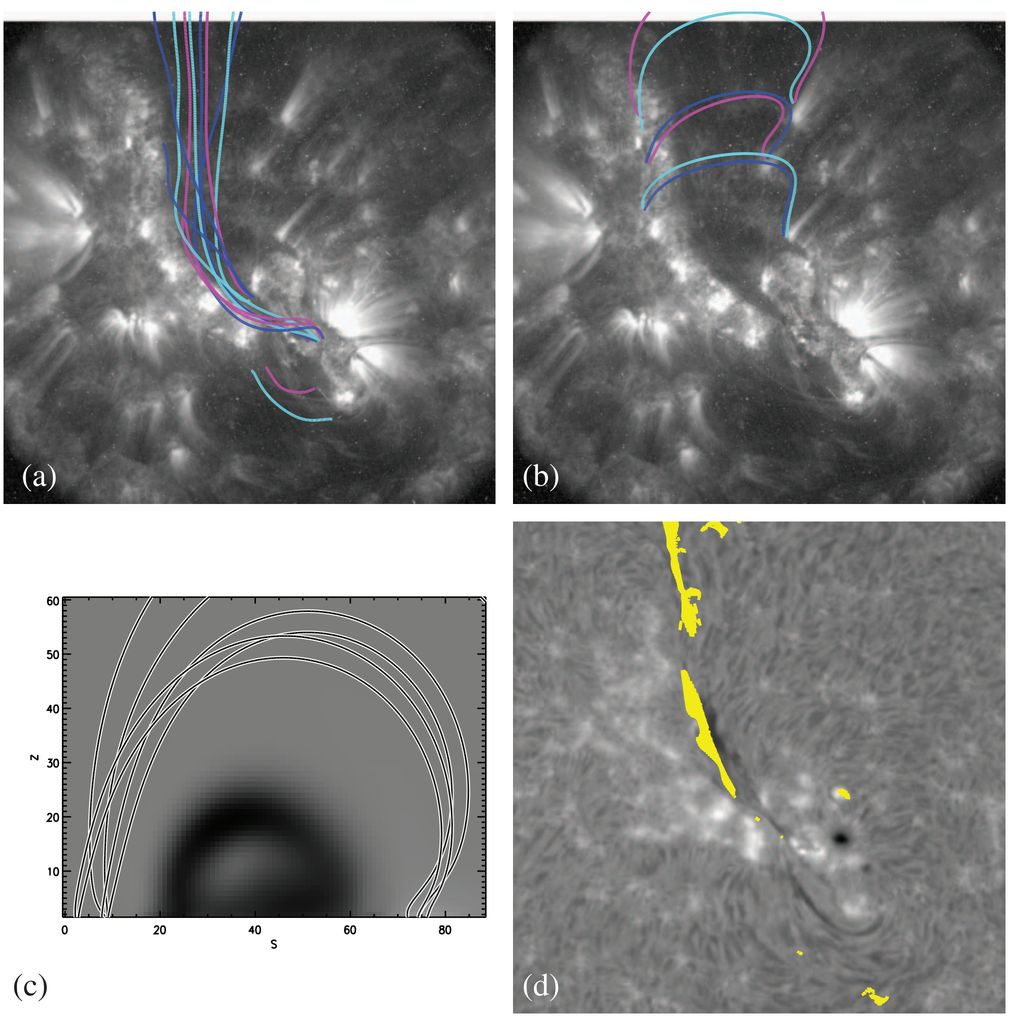

Fig. 7.—Model for NOAA 10005 (model 11). (*a*) Field lines in the modeled flux rope, superposed on the *TRACE* image. (*b*) Field lines in overlying coronal arcade. Note that the western leg of the highest latitude loop matches the observed EUV structure. (*c*) Hollow core distribution of electric currents in a vertical cross section of the flux rope, and field lines from overlying arcade. (*d*) Dips in magnetic field lines superposed on the Hα image. FOV in panels (*a*), (*b*), and (*d*) is 0.5 $R_\odot$. North is up, and west is to the right.

of the magnetofrictional code. However, inside the active region the main flux rope is held down by an overlying coronal arcade, and the field appears to be close to an equilibrium state.

Some of the arcade field lines are shown in Figure 7*b*. Note that the modeled arcade loops are vertically extended compared to the corresponding loops in the potential field (compare Figs. 6*d* and 7*b*). The western legs of the two higher latitude loops show reasonable agreement with the rays seen in the *TRACE* image. The leg of the lower latitude loop still deviates by about 30° from the observed ray structure. We have not been able to construct a model that fits this feature.

Figure 7*c* shows the projection of the arcade field lines in a vertical cross section of the flux rope. The field lines are superposed on a gray-scale image showing the component of the electric current density ***j*** parallel to the flux rope. As in the previous case, the currents have a hollow core distribution with the strongest currents at the interface between the flux rope and its local surroundings. The center of the flux rope has only a weak magnetic twist, so the current density is small. Also, the flux rope is displaced to the right (west) relative to the position ($s = 34$) where the flux rope was initially inserted. This displacement is due to the fact that the photospheric magnetic fields on the eastern side of the PIL are stronger than those on the western side (see Fig. 6*c*), causing the flux rope to be pushed to the west. This explains why the legs of coronal loops some distance away from the PIL are affected. However, the dips in the magnetic field lines, shown in Figure 7*d*, are still located more or less at the original position of the flux rope and show good agreement with the observed Hα filament. Therefore, the interior structure of the flux rope is asymmetric.

We also considered a model with larger axial flux (model 12) but found that the field does not reach an equilibrium in this case. Therefore, the upper limit on the axial flux for this active region is between 14×10^{20} and 22×10^{20} Mx, and model 11 is not far from the upper limit. *TRACE* observed a partial eruption of the flux rope on June 24. The event started at about 15:11 UT, as shown by the opening of a thin loop overlying the flux rope. The flare ribbons are not very bright in *TRACE* 171 Å, but postflare loops are clearly seen at 16:45 UT. The *GOES* satellite observed a small X-ray flare (magnitude C1.4), starting at 15:25 UT and ending at 16:59 UT. Therefore, the flux rope was stable for many hours after the time of the present model but did eventually become unstable.

6. DISCUSSION

We constructed NLFFF models of two active regions and compared the results with *TRACE* and BBSO observations. The modeling used the flux rope insertion method, a procedure for constructing NLFFFs that are highly sheared. An advantage of this method is that measurements of photospheric *vector* magnetic fields are not required, provided that the active region is not too far from disk center. Also, the model field is directly compared with *coronal* observations, which provide the ultimate test of the validity of any 3D magnetic model. However, the method does not provide a unique solution for the 3D magnetic field; in general a range of possible NLFFF models with different flux rope parameters are compatible with the observations. *TRACE* observations indicate that there are also deviations from potential fields at larger heights in active regions (Schrijver et al. 2005), but the present method does not provide the best tool for fitting such observations. The method is not intended to provide a general solution to the problem of modeling active region magnetic fields.

We find that both active regions contain *coronal flux ropes*, i.e., highly sheared, weakly twisted fields that are held down by an overlying coronal arcade. Such flux ropes are needed in order to fit the observed coronal loop structures and Hα filaments. In NOAA 9997/10000 the flux rope is anchored in the active regions at both ends, whereas in NOAA 10005 the flux rope extends onto the quiet Sun to the north of the active region. The axial magnetic flux in these flux ropes is about 14×10^{20} Mx, the magnetic free energy is about 10^{32} ergs, and the relative magnetic helicity is about -3×10^{43} Mx^2. The free energy is sufficient for a large flare, but no X- or M-class flares are observed in these active regions.

The role of helicity in active regions can be better understood by examining the relative helicity H_R for different models in Table 2. Models 1, 2, 3, and 4 show the magnitude of helicity increasing as the axial field is increased. This helicity is mainly associated with magnetic shear, not the commonly thought of tightly coiled flux rope. In model 7 we increase the poloidal flux, so the flux rope becomes more tightly coiled. Note that the helicity in model 4 is still larger than that in model 7. Therefore, it is easier to increase the helicity by strengthening the axial field in a sheared configuration than by twisting up the flux rope. Our preferred model (model 8) has an intermediate value of helicity. We conclude that the helicity is mostly associated with the axial field of the flux rope, not the poloidal field.

The relative helicity is a measure of the linkage of magnetic flux tubes in the system (see Berger & Field 1984). In setting up our models, part of the high-altitude coronal flux is rerouted into a low-lying flux rope, i.e., the linkage of this flux with respect to the remaining coronal flux is changed (see Appendix A). The expected value for the helicity is the product of the fluxes, $|H_R| \approx (\Phi_{\rm AR} - \Phi_{\rm axi})\Phi_{\rm axi}$, where $\Phi_{\rm axi}$ is the axial flux in the flux rope and $\Phi_{\rm AR}$ is the total flux of the active region. Using $\Phi_{\rm AR} = 2.5 \times 10^{22}$ Mx (see Table 1) and $\Phi_{\rm axi} = 1.4 \times 10^{21}$ Mx, we find $|H_R| \approx 3.3 \times 10^{43}$ Mx^2, consistent with the above numerically determined value. Similar values for relative helicity were found in other active regions (Gary et al. 1987; Bleybel et al. 2002; Régnier et al. 2002; Mandrini et al. 2004).

Models with different amounts of axial flux were constructed to determine the conditions for which the flux rope can be stably held down by the overlying coronal arcade. For NOAA 9997/10000 we found that the maximum axial flux is about 15×10^{20} Mx. For NOAA 10005 we predict that a flux rope with an axial flux of 22×10^{20} Mx would no longer be stable. Therefore, in both cases *the flux ropes are close to the upper limit of the axial flux* that can be stably supported by the active regions. Note that the upper limit is less than 10% of the flux of the active region, so the amount of axial flux necessary to destabilize an active region is relatively small. No large flares occurred in these active regions for several days before or after the present observations, and only a small eruption was observed for NOAA 10005.

For NOAA 9997/10000 we found that models with small poloidal flux produce better agreement with observations than a model with larger poloidal flux. Therefore, the magnetic field at the center of the flux rope is only weakly twisted. The electric currents in the flux rope run mainly at the interface between the flux rope and its local surroundings, not uniformly distributed over the cross section of the flux rope (Titov & Démoulin 1999) or concentrated in a thin current filament (e.g., Lin & Forbes 2000; Lin et al. 2002). The average twist angle of the flux rope can be defined as $\theta \equiv 2\pi F_{\rm pol} L/\Phi_{\rm axi}$, where $F_{\rm pol}$ is the poloidal flux per unit length along the flux rope, $\Phi_{\rm axi}$ is the axial flux, and L is the length of the flux rope. In NOAA 9997/10000 the twist angle along the eastern section of the flux rope is about 0.9 rad, significantly less than the threshold for kink instability (Hood & Priest 1981; Török et al. 2004; Birn et al. 2006). Therefore, the flux rope is expected to be stable to kink modes. However, as discussed above, the flux rope is close to the upper limit on the axial flux. This suggests that injection of additional axial flux may result in a "catastrophic loss of equilibrium" (Lin & Forbes 2000) in which the flux rope pushes through the overlying coronal arcade and erupts. The fact that no such event is observed for this active region suggests that the excess energy present in these flux ropes can be released gradually and does not require a large eruptive event.

In our NLFFF models, the regions at large height above the flux rope are nearly current-free, $\boldsymbol{j} \approx 0$. However, the magnetic field $\boldsymbol{B}$ in these regions is not exactly the same as the potential field $\boldsymbol{B}_p$. The reason is that some of the coronal magnetic flux has been diverted into the low-lying flux rope. Therefore, the photospheric magnetic sources at the two ends of the coronal flux rope no longer contribute to the high-altitude field, as they do in a potential field. For example, in model 8 the direction of $\boldsymbol{B}$ in the coronal arcade overlying the flux rope differs from the direction of $\boldsymbol{B}_p$ by about 10°. Therefore, when comparing high-altitude coronal loops with potential field models (e.g., Schrijver et al. 2005), one should keep in mind that a small difference in the orientations of observed loops and computed field lines may be due to low-lying flux ropes and does not imply that electric currents are present at large height in the corona.

The *TRACE* 171 Å images are sensitive only to plasmas in a narrow temperature range near 1 MK and are not well suited to the task of finding sheared fields near PILs. In the future, we plan to use data from the *Hinode* X-Ray Telescope (XRT), which is sensitive to a much broader range of temperatures. XRT observations may put stronger observational constraints on NLFFF models of nonflaring active regions. Future missions such as the *Solar Dynamics Observatory* (*SDO*) will provide a wealth of data on coronal loop structures. To extract information on nonpotentiality and coronal electric currents from such data, more advanced techniques for modeling the coronal field are needed. The present approach is only a first step in this direction.

The authors would like to thank the referee for their detailed comments and suggestions that have resulted in a greatly improved paper. The authors would also like to thank Vasyl Yurchyshyn for providing many Hα images from the Big Bear Solar Observatory. This work was supported by NASA/LWS grant NNG05GK32G. *TRACE* data analysis at SAO is supported by a contract from Lockheed Martin.

APPENDIX A

FLUX ROPE INSERTION METHOD

In this appendix we describe a method for constructing NLFFF models containing flux ropes. The computational domain is a wedge-shaped volume in the corona surrounding an observed active region or filament. We use a spherical coordinate system (r, θ, ϕ), where r is the radial distance from Sun center, θ is the polar angle (also known as colatitude angle), and ϕ is the azimuth angle. The computational domain extends from the photosphere ($r = R_\odot$) to a "source surface" at $r \sim 2\ R_\odot$ where the magnetic field is assumed to be radial. The magnetic field is described in terms of the vector potential $\boldsymbol{A}(\boldsymbol{r})$, where $\boldsymbol{B} \equiv \nabla \times \boldsymbol{A}$, and the three components of the vector $\boldsymbol{A}$ are defined on staggered grids, so that $\nabla \cdot \boldsymbol{B} = 0$ is algebraically satisfied (see van Ballegooijen et al. 2000). The grid is defined in terms of the variables (x, y, z):

$$x = \frac{\phi}{\Delta\phi}, \qquad y = -\frac{1}{\Delta\phi} \ln\left[\tan\left(\frac{\theta}{2}\right)\right], \qquad z = \frac{1}{\Delta\phi} \ln\left(\frac{r}{R_\odot}\right), \tag{A1}$$

where $\Delta\phi$ is the azimuthal grid spacing in the photosphere in radians. The present version of the code uses variable grid spacing: In the low corona $\delta x = \delta y = \delta z = 1$, so that the physical size of the unit cell is $h_\theta = h_\phi = r \sin\theta\Delta\phi$, and $h_r = r\Delta\phi$. At larger heights the spacing is doubled, $\delta x = \delta y = \delta z = 2$, 4, and 8, starting at heights $z = 30$, 60, and 120, respectively. The purpose of this variable grid spacing is to minimize the number of grid points required to cover a large coronal volume, while maintaining high spatial resolution on the photosphere. For example, the full-disk MDI magnetograms have a nominal plate scale of $1.97''$ pixel^{-1}, or about 0.002 $R_\odot$. Therefore, to resolve small magnetic features in MDI magnetograms requires $\Delta\phi \sim 0.002$ rad or better.

The radial component of magnetic field at the photosphere, $B_r(R_\odot, \theta, \phi)$, is derived from observations. For the models presented in this paper we use MDI magnetograms, which provide only the line-of-sight component of magnetic field, $B_\parallel$. We approximate $B_r \approx B_\parallel$, which is valid near solar disk center but becomes increasingly inaccurate as we move away from disk center. The error is especially large in sunspot penumbrae, where the magnetic field is highly inclined with respect to the radial direction. Therefore, we require that the sunspots are no more than 15° away from disk center in heliocentric angle. Outside sunspots the photospheric magnetic field is nearly radial; therefore, within 37° from disk center the approximation $B_r \approx B_\parallel$ is accurate to about 20%. This level of accuracy is sufficient for the models presented here, but future modeling would benefit from the use of vector magnetograms.

When high-cadence MDI data are available, up to five magnetograms are averaged together to increase the signal-to-noise ratio. When both high-resolution and full-disk magnetograms are available, the full-disk magnetogram is mapped onto $B_r(R_\odot, \theta, \phi)$ first, then the appropriate pixels are replaced with values mapped from the high-resolution magnetogram. For the models presented here, the base field was constructed by averaging magnetograms taken within a 5 minute period. For active region NOAA 9997/10000 the extracted field has a large flux imbalance, corresponding to an average radial field of +5 G at the photosphere. For NOAA 10005 we enhanced the positive polarity fields such that the open flux in the domain is $+6 \times 10^{20}$ Mx and the sunspot has a peak field strength of 3300 G.

Next, the path of the flux rope is selected by manually tracing an Hα filament on a BBSO image. The curve starts in a region of positive polarity near the PIL, follows the path of the observed filament, and ends in a region with negative polarity on the opposite side of the PIL. Figure 1*b* shows the filament path on 2002 June 18. We also measure the photospheric magnetic fluxes Φ_1 and Φ_2 contained in two circular areas at the start and end points. The flux rope will be anchored in the photosphere at the two ends of the selected curve. The locations of the start and end points determine the *chirality* of the flux rope, i.e., its dextral or sinistral orientation with respect to the surrounding magnetic fields (Martin et al. 1994; Martin 1998). The chirality appropriate for each filament was determined from the direction of the observed Hα fibrils near the PIL (Foukal 1971). The axial and poloidal fluxes of the flux rope are selected by trial and error, based on how well the final model fits the observations. The axial flux Φ_{axi} must be greater than or equal to the photospheric fluxes $|\Phi_1|$ and $|\Phi_2|$. A negative magnetic source $-\Phi_{axi}$ is added to the photospheric magnetic map at the starting point of the selected path, and a positive source $+\Phi_{axi}$ is added at the end point. The purpose of these sources is to counter the effect of the flux rope (see below).

The next step is to compute the vector potential $\boldsymbol{A}(\boldsymbol{r})$ of the *potential* field based on the modified magnetic map. The method for computing potential fields in a domain that is part of a spherical shell is described in Appendix B of van Ballegooijen et al. (2000). The gauge of $\boldsymbol{A}$ is chosen such that $A_r(r, \theta, \phi) = 0$. Then an elongated *cavity* is created along the selected filament path. This is done by setting $\boldsymbol{A}(r, \theta, \phi) = (R_\odot/r)\boldsymbol{A}(R_\odot, \theta, \phi)$ in a volume above the selected path, where $\boldsymbol{A}(R_\odot, \theta, \phi)$ is the vector potential on the photosphere. Since $A_r = 0$, the horizontal components of magnetic field vanish in the cavity ($B_\theta = B_\phi = 0$). The above procedure has the effect of pushing horizontal fields to the top of the cavity, leaving only the vertical fields associated with flux located at its base. Since the path is chosen to be along the PIL, these vertical fields are weak and the cavity is nearly field free. For the models discussed in this paper the cavity width is 8 cells and the cavity height is 16 cells (NOAA 9997/10000) or 11 cells (NOAA 10005).

The flux rope can now be inserted into this (nearly field-free) cavity. The rope consists of two spatially distinct components: a thin horizontal tube that represents the axial field of the flux rope, and a set of flux rings that are wrapped around the tube and represent the poloidal field. The height z_0 of the flux rope is generally taken to be 5–12 cells. At the two ends of the path the flux rope connects to the photosphere via two short vertical sections. The radial fluxes in these vertical sections counteract the additional sources. Therefore, when the flux rope is inserted into the model, the original observed photospheric flux distribution is restored.

Inserting the flux rope into the model involves modifying components of the $\boldsymbol{A}$ vectors in the computational domain. These components are defined at the middle of each of the 12 edges of a unit cell. The selected filament path generally crosses the edges of the cells at the base of the computational domain. Inserting the axial flux involves modifying A_θ and A_ϕ at all horizontal edges between the photosphere ($z = 0$) and the flux rope axis ($z = z_0$). The new value is $A_{new} = A_{old} + \Phi_{axi}h^{-1}(z)$, where Φ_{axi} is the user-defined axial flux and $h(z)$ is the horizontal size of the cells. This procedure ensures that $\nabla \times \boldsymbol{A} \approx 0$ at all points in the cavity except inside the flux rope, where $\nabla \times \boldsymbol{A} = \boldsymbol{B}$. By manipulating the $\boldsymbol{A}$ vectors in this manner, shear is created only inside the flux rope, where it is desired. Inserting the poloidal flux rings involves modifying the components of the $\boldsymbol{A}$ vectors in both the flux rope and a 2 cell annulus around the flux rope such that $\boldsymbol{A}_{new} = \boldsymbol{A}_{old} + F_{pol}\hat{\boldsymbol{s}}$, where F_{pol} is the user-defined poloidal flux and $\hat{\boldsymbol{s}}$ is the direction along the flux rope axis. The resulting field has $\nabla \cdot \boldsymbol{A} \neq 0$ in and near the flux rope.

Finally, we use magnetofrictional relaxation (Yang et al. 1986; van Ballegooijen 2004) in order to drive the magnetic field toward a force-free state. During the early stages of this relaxation process, we use resistive diffusion in order to meld together the axial and poloidal fields of the flux rope. After this initial phase, the vector potential is evolved according to the following equation:

$$\frac{\partial \boldsymbol{A}}{\partial t} = \boldsymbol{v} \times \boldsymbol{B} + \frac{\boldsymbol{B}}{B^2}\nabla \cdot \left(\eta_4 B^2 \nabla \alpha\right) + \nabla(\eta_d \nabla \cdot \boldsymbol{A}), \tag{A2}$$

where $\boldsymbol{v}$ is the plasma velocity, η_4 and η_d are constants, and $\alpha \equiv \boldsymbol{j} \cdot \boldsymbol{B}/B^2$, where $\boldsymbol{j} = \nabla \times \boldsymbol{B}$. The velocity is given by

$$\boldsymbol{v} = (f\boldsymbol{j} - v_1\hat{\boldsymbol{r}} \times \boldsymbol{B}) \times \boldsymbol{B}/B^2, \tag{A3}$$

where f is the coefficient of magnetofriction. The relaxation process causes the flux rope to expand and the surrounding arcade to contract, so the cavity quickly disappears, and the final results do not depend on the initial size of the cavity.

The quantity v_1 in equation (A3) is an additional upward velocity that is present only in the photosphere (level $z = 1$). This velocity simulates the effects of magnetic buoyancy on the flux elements in the photosphere, where the field is not expected to be force-free (Metcalf et al. 2007). The second term in equation (A2) describes hyperdiffusion, a type of magnetic diffusion that conserves magnetic helicity (Boozer 1986; Bhattacharjee & Hameiri 1986). Such diffusion has been used in modeling the evolution of the coronal field (van Ballegooijen & Mackay 2007), but here it is included in order to smooth out numerical artifacts in the electric current distribution, so that the Lorentz force $\boldsymbol{j} \times \boldsymbol{B}$ is accurately determined. The third term in equation (A2) is included in order to suppress numerical artifacts associated with $\nabla \cdot \boldsymbol{A} \neq 0$ in the initial configuration. The effect of this term is to make $\nabla \cdot \boldsymbol{A} \approx 0$ in the final state. At the lower boundary, only the third term is present, with $\nabla \cdot \boldsymbol{A}$ replaced by $\nabla_\perp \cdot \boldsymbol{A}_\perp$, where $\perp$ refers to the horizontal component. Therefore, the radial magnetic field B_r at the photosphere remains unchanged during the relaxation process. We also use periodic boundary conditions in longitude, closed boundaries in latitude, and open boundary conditions at the top, where the field is assumed to be radial.

The magnetic energy always decreases with iteration number. Either the field approaches a nonlinear force-free state ($\boldsymbol{v} = 0$), or the field expands indefinitely toward an open state. The latter occurs when the axial and/or poloidal fluxes of the rope are too large compared with the flux of the overlying arcade. Convergence is monitored by plotting histograms of the angle between the vectors $\boldsymbol{j}$ and $\boldsymbol{B}$. We also plot the Lorentz force along a horizontal or vertical line through the flux rope and compare the net force with its contributions from magnetic pressure and tension. This provides a local diagnostic of the residual forces in the model. Typically, 10^4 iterations are required to obtain an NLFFF, which takes about 8 hr using two 2.66 GHz Dual-Core Intel Xeon processors. The final configuration is compared with both Hα observations of the filament and *TRACE* observations of the surrounding corona. The flux rope parameters are manually varied until the shape, size, and fine structures of the flux rope match the observations.

Modeling an NLFFF in this manner has several benefits. First, the model uses line-of-sight magnetograms. The line-of-sight component of the photospheric field can be measured with much greater precision than the transverse field and is not subject to the 180° ambiguity problem. Second, models can be constructed for different values of the axial and poloidal fluxes of the flux rope. The flux rope parameters are manually varied until a good fit to the *TRACE* and BBSO observations is obtained. This lends insight into typical values of axial and poloidal flux in noneruptive filaments. Third, by increasing these fluxes beyond the "observed" values, we can determine the maximum fluxes for which force-free equilibrium is possible. This can tell us whether or not the field is close to an eruption.

APPENDIX B

MAGNETIC ENERGY AND HELICITY

The magnetic energies of the force-free field $\boldsymbol{B}(\boldsymbol{r})$ and the potential field $\boldsymbol{B}_p(\boldsymbol{r})$ are computed as follows:

$$E_c \equiv \int_{V_c} \frac{|\boldsymbol{B}|^2}{8\pi}\, dV, \qquad E_{c,p} \equiv \int_{V_c} \frac{|\boldsymbol{B}_p|^2}{8\pi}\, dV, \tag{B1}$$

where the integration extends over the *coronal* volume V_c, i.e., the wedge that extends from the photosphere up to the source surface. The magnetic free energy is simply the difference between these energies, $\Delta E_c = E_c - E_{c,p}$.

To compute the relative magnetic helicity (Berger & Field 1984), we must also consider the subsurface volume V_b, i.e., the wedge that extends from the photosphere down to the center of the Sun. Of course, we do not know the subsurface magnetic field, but Berger & Field (1984) have shown that this is not necessary. Let $\boldsymbol{B}_1(\boldsymbol{r})$ and $\boldsymbol{B}_2(\boldsymbol{r})$ be two fields defined over the entire volume $V\,(=V_b \cup V_c)$. In the corona $\boldsymbol{B}_1 = \boldsymbol{B}$ and $\boldsymbol{B}_2 = \boldsymbol{B}_p$, while in the subsurface layers $\boldsymbol{B}_1 = \boldsymbol{B}_2$, an arbitrary field that matches the observed B_r in the photosphere. It follows that in the subsurface layers $\boldsymbol{A}_1 - \boldsymbol{A}_2 = \nabla\chi$, where $\chi(\boldsymbol{r})$ is a scalar function. Then the relative helicity is given by

$$\begin{aligned} H_R &\equiv \int_V (\boldsymbol{A}_1 \cdot \boldsymbol{B}_1 - \boldsymbol{A}_2 \cdot \boldsymbol{B}_2)\, dV \\ &= \int_{V_c} \left(\boldsymbol{A} \cdot \boldsymbol{B} - \boldsymbol{A}_p \cdot \boldsymbol{B}_p\right) dV + \int_S \chi B_r\, dS, \end{aligned} \tag{B2}$$

where the last integral is over the photospheric surface S. In our models, the vector potential $\boldsymbol{A}(R_\odot, \theta, \phi)$ for the NLFFF is not equal to that of the potential field; therefore, $\chi \neq 0$ and the surface integral in equation (B2) cannot be neglected. We compute $\chi(\theta, \phi)$ by integration of $\boldsymbol{A} - \boldsymbol{A}_p$ over the photosphere. The helicity values are given in Tables 2 and 3. These results neglect possible contributions to the relative helicity from changes in $\boldsymbol{A}$ at the upper boundary of the computational domain.

REFERENCES

Acton, L., et al. 1992, Science, 258, 591
Antiochos, S. K., MacNiece, P. J., & Spicer, D. S. 2000, ApJ, 536, 494
Aulanier, G., & Démoulin, P. 1998, A&A, 329, 1125
Berger, M. A., & Field, G. B. 1984, J. Fluid Mech., 147, 133
Bhattacharjee, A., & Hameiri, E. 1986, Phys. Rev. Lett., 57, 206
Birn, J., Forbes, T. G., & Hesse, M. 2006, ApJ, 645, 732
Bleybel, A., Amari, T., van Driel-Gesztelyi, L., & Leka, K. D. 2002, A&A, 395, 685
Boozer, A. H. 1986, J. Plasma Phys., 35, 133
Canfield, R. C., Hudson, H. S., & McKenzie, D. E. 1999, Geophys. Res. Lett., 26, 627
Démoulin, P., Hénoux, J. C., Priest, E. R., & Mandrini, C. H. 1996, A&A, 308, 643
Foukal, P. 1971, Sol. Phys., 19, 59
Gary, G. A., Moore, R. L., Hagyard, M. J., & Haisch, B. M. 1987, ApJ, 314, 782
Handy, B. N., et al. 1999, Sol. Phys., 187, 229
Hood, A. W., & Priest, E. R. 1981, Sol. Phys., 73, 289
Karpen, J. T., Antiochos, S. K., Hohensee, M., Klimchuk, J. A., & MacNiece, P. J. 2001, ApJ, 553, L85
Karpen, J. T., Tanner, S. E. M., Antiochos, S. K., & DeVore, C. R. 2005, ApJ, 635, 1319
Lin, J., & Forbes, T. G. 2000, J. Geophys. Res., 105, 2375
Lin, J., van Ballegooijen, A. A., & Forbes, T. G. 2002, J. Geophys. Res., 107, SSH 3-1, DOI: 10.1029/2002JA009486
Mandrini, C. H., Démoulin, P., van Driel-Gesztelyi, L., Green, L. M., & López Fuentes, M. C. 2004, Ap&SS, 290, 319
Martin, S. F. 1998, Sol. Phys., 182, 107
Martin, S. F., Bilimoria, R., & Tracadas, P. W. 1994, in Solar Surface Magnetism, ed. R. J. Rutten & C. J. Schrijver (Dordrecht: Kluwer), 303
McClymont, A. N., Jiao, L., & Mikic, Z. 1997, Sol. Phys., 174, 191
Metcalf, Th. R., et al. 2007, Sol. Phys., submitted
Mikic, Z., & McClymont, A. N. 1994, in ASP Conf. Ser. 68, Solar Active Region Evolution: Comparing Models with Observations, ed. K. S. Balasubramaniam & G. W. Simon (San Francisco: ASP), 225
Pevtsov, A. A., Canfield, R. C., & McClymont, A. N. 1997, ApJ, 481, 973
Pevtsov, A. A., Canfield, R. C., & Metcalf, T. R. 1995, ApJ, 440, L109
Priest, E. R., & Forbes, T. G. 2002, A&A Rev., 10, 313
Régnier, S., Amari, T., & Kersalé, E. 2002, A&A, 392, 1119
Rust, D. M., & Kumar, A. 1996, ApJ, 464, L199
Scherrer, P. H., et al. 1995, Sol. Phys., 162, 129
Schrijver, C. J. 2007, ApJ, 655, L117
Schrijver, C. J., DeRosa, M. L., Title, A. M., & Metcalf, T. R. 2005, ApJ, 628, 501
Schrijver, C. J., et al. 2006, Sol. Phys., 235, 161
Sterling, A. C., Hudson, H. S., Thompson, B. J., & Zarro, D. M. 2000, ApJ, 532, 628
Titov, V. S., & Démoulin, P. 1999, A&A, 351, 707
Török, T., Kliem, B., & Titov, V. S. 2004, A&A, 413, L27
Valori, G., Kliem, B., & Keppens, R. 2005, A&A, 433, 335
van Ballegooijen, A. A. 2004, ApJ, 612, 519
van Ballegooijen, A. A., DeLuca, E. E., Squires, K., & Mackay, D. H. 2007, J. Atmos. Terr. Phys., 69, 24, DOI:10.1016/j.jastp.2006.06.007
van Ballegooijen, A. A., & Mackay, D. H. 2007, ApJ, 659, 1713
van Ballegooijen, A. A., Priest, E. R., & Mackay, D. H. 2000, ApJ, 539, 983
Wheatland, M. S. 2006, Sol. Phys., 238, 29
Wheatland, M. S., Sturrock, P. A., & Roumeliotis, G. 2000, ApJ, 540, 1150
Wiegelmann, T. 2004, Sol. Phys., 219, 87
Wiegelmann, T., Inhester, B., & Sakurai, T. 2006, Sol. Phys., 233, 215
Yang, W. H., Sturrock, P. A., & Antiochos, S. K. 1986, ApJ, 309, 383